Monthly Notices of the ROYAL ASTRONOMICAL SOCIETY

MNRAS **507,** 1202–1215 (2021) https://doi.org/10.1093/mnras/stab2209
Advance Access publication 2021 July 31

Inferring the concentration of dark matter subhaloes perturbing strongly lensed images

Quinn Minor [1,2]★ Manoj Kaplinghat,[3] Tony H. Chan[4] and Emily Simon[5]

[1]*Department of Science, Borough of Manhattan Community College, City University of New York, New York, NY 10007, USA*
[2]*Department of Astrophysics, American Museum of Natural History, New York, NY 10024, USA*
[3]*Department of Physics and Astronomy, University of California, Irvine, CA 92697, USA*
[4]*Department of Physics, City College of New York, New York, NY 10031, USA*
[5]*Department of Astronomy, Columbia University, New York, NY 10027, USA*

Accepted 2021 July 20. Received 2021 June 30; in original form 2020 December 1

ABSTRACT

We demonstrate that the perturbations of strongly lensed images by low-mass dark matter subhaloes are significantly impacted by the concentration of the perturbing subhalo. For subhalo concentrations expected in Lambda cold dark matter (ΛCDM), significant constraints on the concentration can be obtained at *Hubble Space Telescope* (*HST*) resolution for subhaloes with masses larger than about $10^{10}\,M_\odot$. Constraints are also possible for lower mass subhaloes, if their concentrations are higher than the expected scatter in CDM. We also find that the concentration of lower mass perturbers down to $\sim 10^8\,M_\odot$ can be well constrained with a resolution of ∼0.01 arcsec, which is achievable with long-baseline interferometry. Subhalo concentration also plays a critical role in the detectability of a perturbation, such that only high-concentration perturbers with mass $\lesssim 10^9\,M_\odot$ are likely to be detected at *HST* resolution. If scatter in the ΛCDM mass–concentration relation is not accounted for during lens modelling, the inferred subhalo mass can be biased by up to a factor of 3 (6) for subhaloes of mass $10^9\,M_\odot$ ($10^{10}\,M_\odot$); this bias can be eliminated if one varies both mass and concentration during lens fitting. Alternatively, one may robustly infer the projected mass within the subhalo's perturbation radius, defined by its distance to the critical curve of the lens being perturbed. With a sufficient number of detections, these strategies will make it possible to constrain the halo mass–concentration relation at low masses in addition to the mass function, offering a probe of dark matter physics as well as the small-scale primordial power spectrum.

Key words: gravitational lensing: strong – galaxies: dwarf – dark matter.

1 INTRODUCTION

A key prediction of the cold dark matter (CDM) paradigm is the existence of a large number of dark matter subhaloes around galaxies, with masses that go down to $< 1\,M_\odot$ for the smallest haloes (Green, Hofmann & Schwarz 2004). The vast majority of these subhaloes are expected to be entirely devoid of stars, as their primordial gas would have been heated sufficiently by the ultraviolet background during reionization to escape the shallow potential wells of these subhaloes. In the past few years, hydrodynamical cosmological simulations that include radiative transfer effects have estimated that star formation is suppressed entirely in dark matter haloes with virial masses lower than 10^8–$10^9\,M_\odot$ (Sawala et al. 2016), where the exact threshold depends on the details of the gas heating and cooling. The observed ultrafaint satellites of the Milky Way Galaxy, such as those recently discovered in the Dark Energy Survey (Bechtol et al. 2015), are thus expected to inhabit dark matter haloes that lie just above this threshold (Brown et al. 2014). Detecting a large population of dark matter haloes with masses $\lesssim 10^9\,M_\odot$ is thus a crucial test of CDM.

Many well-motivated particle models for dark matter diverge from the CDM paradigm, with very different predictions for small-scale structure. For example, in warm dark matter models, the thermal motion of free-streaming dark matter particles erased small-scale structure before non-linear collapse would have occurred; as a result, the number of dark matter subhaloes is suppressed below a particular mass threshold (typically below $\sim 10^9\,M_\odot$ for viable models; Bose et al. 2017), and galaxies form with lower central densities (Lovell et al. 2014). In hidden sector models, dark matter particles can interact among themselves via a hidden force (Feng et al. 2009). A sufficiently high self-interaction cross-section can lower the central density of low-mass haloes and subhaloes compared to that of CDM (Rocha et al. 2013; Elbert et al. 2015). However, the particle model of dark matter is not the only possible factor that can alter the small-scale matter power spectrum: certain types of inflation models can produce a running (departure from power law) in the primordial power spectrum (Ashoorioon & Krause 2006; Kobayashi & Takahashi 2011; Minor & Kaplinghat 2015), suppressing power at small scales (Garrison-Kimmel et al. 2014). Whether primordial or through late-time effects, all of these alternative cosmological paradigms make distinct predictions for both the abundance and central densities of dark matter haloes of a given mass.

Strong gravitational lensing provides a powerful probe of the dark matter distribution on dwarf galaxy scales, since the lensed images of a background source can undergo visible perturbations due to

★ E-mail: qminor@bmcc.cuny.edu

the presence of dark matter subhaloes as well as dark matter haloes that lie along the line of sight to the lens galaxy. Recently, a few detections of dark substructures in gravitational lenses have been reported by observing their effect on highly magnified images. Two of these were discovered in the Sloan Lens ACS (SLACS) data set (Vegetti et al. 2010, 2012), while, more recently, a subhalo was reported by Hezaveh et al. (2016b) to have been detected in the lens system SDP.81 (ALMA Partnership 2015). In order to test the expected mass function of haloes in CDM, a robust estimate of the mass of these perturbing dark matter haloes is very important; unfortunately, however, the total inferred mass of the perturbers is highly dependent on their assumed density profile and tidal radius (Vegetti et al. 2014; Minor, Kaplinghat & Li 2017). One approach to test CDM is to simply assume that the perturbers follow a Navarro–Frenk–White (NFW) profile (or a truncated form thereof), since the dark matter haloes in CDM *N*-body simulations are well fitted by this profile (Navarro, Frenk & White 1996). This approach is supported by recent results from hydrodynamical simulations that subhaloes below $10^9\,\mathrm{M}_\odot$ are near the threshold for star formation and hence may not be significantly altered by baryon physics (Ocvirk et al. 2016; Sawala et al. 2016; Fitts et al. 2017). Even under this assumption, however, there is some expected scatter in the central density of haloes of a given mass, embodied by the concentration parameter $c_{200} = r_{200}/r_\mathrm{s}$; hence, assuming that subhaloes follow a tight mass–concentration relation without scatter may also bias the inferred masses.

Estimating the mass of a perturbing subhalo is not the only quantity of importance, however. We argue that constraining the concentration of perturbing dark matter subhaloes is equally important as the total mass, since different particle models for dark matter (or even inflation physics) can differ widely in their predictions for the central densities of dark matter haloes (Rocha et al. 2013; Lovell et al. 2014). Thus, an important question is whether the concentration of perturbing dark matter haloes can be meaningfully constrained in addition to their masses. If the perturber's concentration significantly affects the strength of the perturbation to the local lensing deflection, then in principle meaningful constraints on the concentration are possible. Indeed, recently, Gilman et al. (2020) have shown that constraints on subhalo concentrations are possible for lensed quasars, at least in a statistical sense. If concentrations of individual subhaloes can be constrained from their perturbations of lensed arcs, this approach may not only achieve a more robust mass estimate, but also provide an additional probe of the small-scale power spectrum beyond simply testing the CDM halo mass function.

In this paper, we simulate and model hundreds of mock lensing data to investigate the effect of dark matter subhalo concentration on lensing perturbations. We show that constraints on dark matter subhalo concentrations are indeed possible, and provide a powerful probe of the small-scale matter power spectrum. In addition, we will show that making the approximation that subhaloes follow an exact mass–concentration relation (without scatter) during modelling of substructure perturbations can result in biased mass inferences, by up to a factor of ∼6 or so. Hence, even if dark matter is indeed cold and collisionless, scatter in the mass–concentration relation cannot be ignored if one aims to test the expected CDM halo mass function at dwarf galaxy scales via strong lensing.

We organize the paper as follows: in Section 2, we describe our lens modelling software and simulated data. In Section 3, we investigate how well the perturber's concentration can be constrained, both at *Hubble Space Telescope* (*HST*) resolutions and at higher resolutions expected from next-generation telescopes. In Section 4, we will investigate the effect of halo concentration on the detectability of substructure perturbations. In Section 5, we will discuss the physical interpretation of the degeneracy between mass and concentration in terms of the size of the subhalo's lensing perturbation. In Section 6, we explore the effect of concentration/mass on the uncertainties in the subhalo's inferred position, projected mass, and density slope. Next, in Section 7.1, we explore the expected bias (in CDM) in the inferred perturber's mass if scatter in halo concentration is unaccounted for, while in Section 7.2 we demonstrate that bias in these cases is eliminated by using the mass estimator of Minor et al. (2017). Finally, in Section 8, we discuss the physical interpretation of the concentration constraints, and in Section 9 we discuss the effect of tidal stripping on our results. We conclude in Section 10.

2 LENS MODELLING AND MOCK DATA

2.1 Lens simulation and modelling procedure

To investigate the effect of subhalo concentration, we generate a grid of mock data that explores a variety of different subhalo masses, concentrations, positions in the lens plane, and lens redshifts. For the primary lens, we use a power-law ellipsoidal projected density profile, plus an external shear term in the potential. We adopt parameters such that it closely resembles the lens SDSSJ0946+1006, for which Vegetti et al. (2010) detected a perturbing subhalo. For our primary mock data grid, we generate simulated images using the pixel size of the *Hubble Space Telescope* (*HST*) ACS camera (0.045 arcsec) and the actual *HST* point spread function (PSF) pixel map used by Vegetti et al. (2010). For a small subset of these data, we will also generate and model a high-resolution version with 0.01 arcsec pixel size (described in Section 3.2). The source galaxy is created using an elliptical Gaussian profile with two possible sizes, corresponding to unlensed widths of 0.03 and 0.06 arcsec.

In our primary mock data images, the subhalo is modelled using a spherical NFW profile (Navarro et al. 1996), without any tidal truncation. As we show in Section 9, for the majority of subhalo perturbations, we expect the subhalo's tidal radius to be much larger than its NFW scale radius, since the most subhaloes will be several tens to hundreds of kiloparsecs away from the host galaxy centre (Minor et al. 2017). Since the Einstein radius of the lens typically corresponds to a few kiloparsecs in the lens plane, most of that distance lies along the line of sight to the lens plane, i.e. the plane containing the centre of the host galaxy. Thus, in most cases, the tidal radius will not affect the lensing dramatically; however, we will investigate the effect of tidal truncation in detail in Section 9.

Since the Hubble PSF is relatively undersampled compared to the pixel size, the images produced can be sensitive to how the ray tracing is done, particularly near the critical curve. To mitigate this, we split each image pixel into $N \times N$ subpixels and ray trace the centre point of each subpixel to the source plane, assigning it the surface brightness given by the source profile at the position of the ray-traced point. These surface brightness values are then averaged to find the surface brightness of the image pixel. After the ray tracing is complete, the resulting pixel values are then convolved with the PSF and Gaussian noise is added (such that the signal-to-noise ratio is roughly similar to that of the *HST* image of SDSSJ0946+1006) to generate the mock image. An example with a $10^{10}\,\mathrm{M}_\odot$ perturber is shown in Fig. 1. We find that 3×3 splitting achieves sufficient accuracy without adding too much computational burden; a greater number of subpixels change the surface brightness values very little while adding significant computational cost.

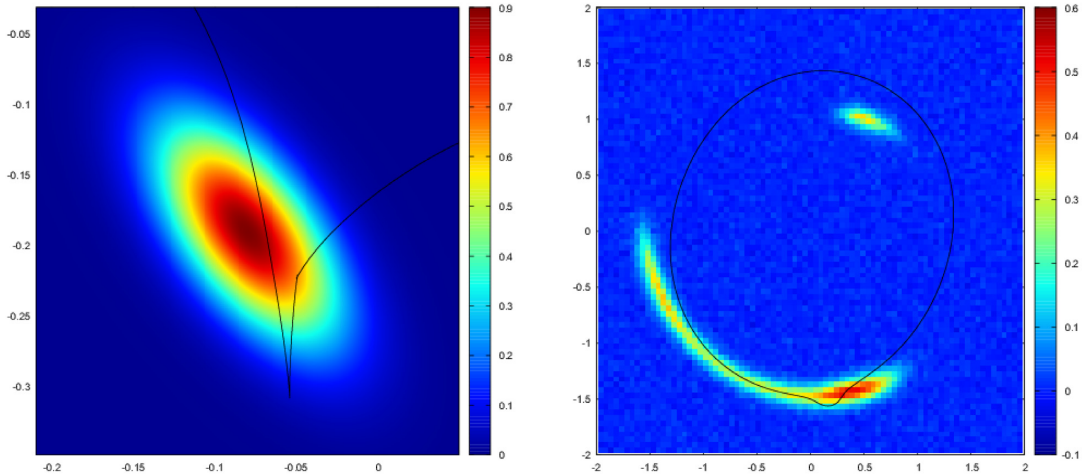

(a) mock source (b) mock data image

Figure 1. Mock source and data image, with a $10^{10}\,M_{\odot}$ perturber. In panel (a), the mock source is shown with caustic overlaid; note the kink in the caustic generated by the perturbing subhalo. In panel (b), the mock image is shown with critical curve overlaid, where a perturbation is evident in the lower arc.

Our primary method for modelling the mock data uses a parametrized surface brightness profile, with the ray tracing as outlined above. This allows for relatively rapid exploration of the parameter space, which consists of both lens and source model parameters, hence reducing computational cost compared to reconstructing pixelated sources. However, for the purposes of constraining the detailed properties of subhaloes, using an elliptical Gaussian profile would be too restrictive a prior, for two reasons: (1) actual galaxies rarely (if ever) have perfectly elliptical contours and Gaussian profiles; (2) even if the true source is Gaussian (as with our mock data), if one is modelling a subhalo with an incorrect mass or concentration, this systematic can often be (at least partially) absorbed into the inferred source galaxy by perturbing the isophotes or deviating from a Gaussian profile. This is also the case if the data are perturbed by a subhalo and one is not including a subhalo in the model at all. Thus, if one does not allow enough freedom in the source galaxy model, the constraints on concentration and mass may appear stronger than they really are.

For our modelling runs where we focus on constraining the concentrations of subhaloes (Sections 3.1 and 3.2), we therefore adopt the following approach: we start with a Sersic profile where the isophotes are 'generalized ellipses' with a radial coordinate defined by

$$r_0(x,y) = \left(|x - x_0|^{C_0+2} + \left| \frac{y - y_0}{q} \right|^{C_0+2} \right)^{\frac{1}{C_0+2}}, \tag{1}$$

where q is the axial ratio and C_0 is the 'boxiness' parameter, such that $C_0 = 0$ corresponds to a perfectly elliptical profile. We then add Fourier mode perturbations to the isophotes, as follows:

$$r(x,y) = r_0(x,y) \left\{ 1 + \sum_{m=1}^{N} [a_m \cos(m\theta) + b_m \sin(m\theta)] \right\}. \tag{2}$$

From experimentation, we find that parameter exploration can become difficult beyond 4–5 Fourier modes, and the $m = 2$ mode is quite degenerate with the axial ratio parameter q. Thus, in our primary fits, we include the modes $m = 1$, 3, 4, 5, 6, with sine and cosine terms for each. For high m modes, fluctuations can easily become quite rapid, leading to noisy source solutions. To regulate this, we switch to the scaled amplitudes $\alpha_m = ma_m$ and $\beta_m = mb_m$, which are the amplitudes of the azimuthal derivative $dr/d\theta$. By using these scaled amplitudes as free parameters, we can set an upper prior limit on the rate of change of the contours that applies equally to all modes. Our method for perturbing the isophotes is essentially identical to that employed by the GALFIT algorithm for fitting galaxy images (Peng et al. 2010), except that instead of including a phase angle parameter, we use the scaled amplitudes for both sine and cosine terms as free parameters; this ensures that there is no coordinate singularity in the limit of very small amplitudes. While our source model may not exhibit all the freedom that a pixelated source does, it none the less allows for a wide range of source morphologies.

The parameter exploration is done using the POLYCHORD algorithm, which is a variant of nested sampling that accommodates a large number of parameters and produces the Bayesian model evidence as well as posterior samples. In each case, the simulated image is first fit without a perturbing subhalo in the model, then the procedure is repeated with a subhalo included in the model. We then calculate the Bayes factor, defined as the ratio of Bayesian evidences $K = \mathcal{E}_{\rm sub}/\mathcal{E}_{\rm no\,sub}$. In practice, we find that a subhalo is detected (such that the posterior includes the correct location of the subhalo) if $K \gtrsim 3$. However, in cases that are just above this threshold (up to $K \sim 10$ or so), there is a large uncertainty in the subhalo's position and mass, and in a few cases multiple modes exist, including one or more fictitious modes in addition to the correct one. Moreover, in real life additional systematics may complicate detection by introducing false positives: the primary lens model may differ from the actual lens profile, e.g. by having non-elliptical contours or twisted isodensity contours, and thus a fictitious subhalo might be preferred to make up these deficiencies. In addition, a more flexible source model (such as source pixel inversion; Suyu et al. 2006; Vegetti & Koopmans 2009) may absorb small lensing perturbations into the source, resulting in a non-detection. With this in mind, for each mock data analysis, we conservatively call the results a detection if the Bayes factor K is greater than 10.

2.2 Mock data grid

The density of subhaloes is parametrized by the concentration $c_{200} \equiv r_{200}/r_{\rm s}$ where r_{200} and $r_{\rm s}$ are the NFW (approximate) virial

radius and scale radius, respectively.[1] When simulating different subhalo concentrations, we aim to cover the expected scatter for a dark matter subhalo's given mass in ΛCDM simulations. For field haloes, *N*-body simulations generally agree that dark matter halo concentrations follow a lognormal distribution with dispersion $\sigma_{\log c} \approx 0.11$ dex, although there have been slight variations in the median concentration of subhaloes of given mass depending on the cosmological model adopted. These differences are generally smaller than the scatter, so for our purposes it is sufficient to adopt a single mass–concentration relation for our mock data, which we take from Dutton & Macciò (2014). Thus for each subhalo, we will choose concentrations according to

$$\log c = \log \bar{c}(M, z) + \Delta_c \sigma_{\log c}, \tag{3}$$

where Δ_c will range from −2 up to 3. The high upper value for Δ_c is motivated by the fact that subhaloes are expected to have slightly higher concentrations compared to field haloes, since more dense subhaloes are more likely to survive tidal stripping.

We justify this as follows. Moliné et al. (2017) found in the Via Lactea and Elvis simulations that the subhalo median concentration is approximately equal to the median value for field haloes, multiplied by a factor $\mathcal{F} = (1 + b \log(x_{\rm sub}))$, where $b = -0.54$ and $x_{\rm sub} = r_{\rm sub}/r_{\rm vir}$ is the ratio of the subhalo's distance from the host galaxy centre to the host galaxy's virial radius. While it is unclear whether this factor differs significantly for large elliptical galaxy hosts, we can at least use it to guide our intuition about what concentrations may be expected among perturbing subhaloes. If we consider subhaloes of median concentration and use $\Delta_c \sigma_{\log c}$ as a proxy for the 'boost' in concentration subhaloes get over field haloes, then we can set $\Delta_c \sigma_{\log c} \approx \mathcal{F}$ and find roughly what $x_{\rm sub}$ corresponds to a given Δ_c. For example, we find that for $\Delta_c = 1\sigma_{\log c}$ above the median field value, the subhaloes are located at ≈0.3 times the virial radius. Many subhaloes are located at or within such a radius, so we can expect that such a boost in concentration is relatively common for subhaloes; in addition, if one assumes that subhaloes experience a similar scatter in concentration as field haloes (Moliné et al. 2017), concentrations 2σ above the median field value should not be uncommon among subhaloes, with a small percentage reaching as high as 3σ above the median. For $\Delta_c = 2\sigma_{\log c}$, one finds that subhaloes are located at ≈0.06 times the virial radius; only a very small fraction of subhaloes lie within this radius. Again, given the scatter, it follows that in CDM only a very small fraction of subhaloes will have concentrations 3σ higher than the median field value.

In view of the above considerations, our mock data grid consists of the following parameter values:

(i) Lens redshift $z_{\rm lens}$: 0.2 and 0.5. We keep the primary lens's Einstein radius the same for either redshift (implying a somewhat more massive primary lens, by roughly a factor of 2.5, at the higher redshift). The source redshift is kept fixed at $z_{\rm src} = 2$.

(ii) Subhalo (untruncated) mass m_{200}: 10^8, 10^9, and 10^{10} $\mathrm{M}_\odot$.

(iii) Subhalo concentration c_{200}, given by equation (3) where Δ_c takes the following values: −2, −1, 0, 1, 2, 3.

[1]Although r_{200} cannot be a reliable approximation to the virial radius of a tidally truncated subhalo, it is nevertheless a straightforward procedure to fit a subhalo using an NFW profile and then calculate r_{200} and m_{200}, which is the virial radius and mass the subhalo *would* have if it were actually a field halo at the given redshift. Thus, a subhalo can be parametrized this way, as long as the parameters are interpreted correctly. This is the approach taken in recent lens modelling studies (Despali et al. 2018; Ritondale et al. 2019) and in analysing subhalo populations in *N*-body simulations (Moliné et al. 2017).

(iv) Subhalo's projected distance from the (unperturbed) critical curve: −0.15, −0.08, −0.01, 0.06, and 0.13 arcsec (where negative values are outside the critical curve, positive values inside). Note, these distances are measured with respect to the nearest point where the critical curve *would* be if there were no perturbation present.

(v) Source size, given by width of Gaussian surface brightness profile σ_s: 0.03 and 0.06 arcsec. We refer to these as 'small' and 'large' source galaxies, respectively. To make a detection more likely, the small source is moved slightly closer to the caustic curve compared to the large source.

In total, we have a grid of 360 mock lenses. In all of our modelling runs, the position of the subhalo $x_{\rm sub}$ and $y_{\rm sub}$ and all of the primary lens parameters are varied freely. We will model the subhalo and source galaxy in three different ways:

(i) **Method 1:** The mass m_{200} and concentration c_{200} are both varied during the fit, and the source is modelled with a Sersic profile with boxiness parameter and five Fourier modes (described in Section 2.1). We focus on these modelling runs in Sections 3.1 and 3.2. Since the more flexible source model increases the computational burden, only a subset of the above mock data are modelled for these sections.

(ii) **Method 2:** The mass m_{200} and concentration c_{200} are both varied during the fit, and the source is modelled with a Gaussian profile. We focus on these modelling runs to explore detectability of perturbations in Sections 4, and the degeneracy between mass and concentration in Section 5.

(iii) **Method 3:** Only the mass m_{200} is varied freely, while the concentration is always set to the median value $\bar{c}(M, z)$ during the fit. The source is modelled with a Gaussian profile. These fits are explored in Sections 7.1 and 7.2.

In all modelling runs, the mass is allowed to vary from 10^6 to 10^{11} $\mathrm{M}_\odot$ and is parametrized as $\log m_{200}$ with a uniform prior over this range (this is equivalent to assuming a logarithmic prior in the subhalo's mass). We use $\log(m_{200}/\mathrm{M}_\odot)$ as our parameter to allow for better initial coverage of the parameter space during the nested sampling, since the subhalo mass ranges over several orders of magnitude during the fit. When varying the concentration, we use c_{200} as our parameter directly with a logarithmic prior in this parameter covering the range (0.5, 100). The host galaxy is modelled with an ellipsoidal power-law profile, where all parameters are varied: b, α, q, θ, x_c, and y_c (the Einstein radius, density log-slope, axial ratio, orientation angle, and centre coordinates, respectively).

3 CONSTRAINTS ON SUBHALO CONCENTRATION AND MASS

3.1 Mass–concentration constraints at *HST* resolution

Since most 10^9 $\mathrm{M}_\odot$ subhaloes and all 10^{10} $\mathrm{M}_\odot$ subhaloes are detected with high significance in our modelling runs, we now investigate the resulting constraints in both mass and concentration for some representative cases. In Fig. 2, we plot joint posteriors in $\log(m_{200}/\mathrm{M}_\odot)$ and c_{200} for subhaloes at $z_{\rm lens} = 0.2$ placed at the closest point to the critical curve (just 0.01 arcsec outside the unperturbed critical curve), for the 'large' source galaxy cases. Posteriors are plotted for 10^9 and 10^{10} $\mathrm{M}_\odot$ subhaloes with concentrations at the median value $\bar{c}(M, z)$ and 2σ above the median in each case.

In all cases, a degeneracy exists between mass and concentration, since a perturbation of similar size can be produced by increasing the mass while decreasing the concentration, or vice versa (this

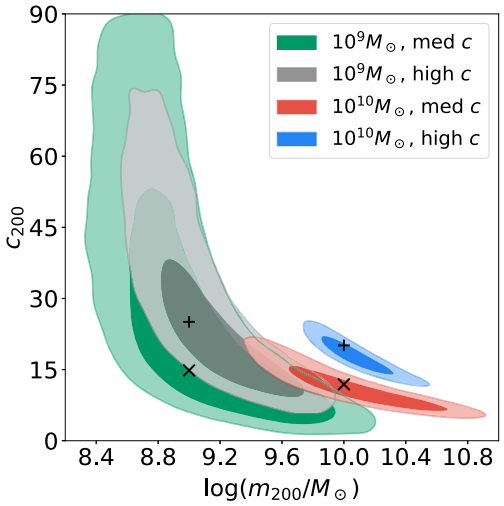

Figure 2. Joint posteriors in log-mass $\log(m_{200}/\,\mathrm{M}_\odot)$ and concentration c_{200} of perturbing subhaloes in four of our mock data fits at *HST* resolution and $z_{\rm lens} = 0.2$. Green and grey contours represent posteriors for $10^9\,\mathrm{M}_\odot$ subhaloes with concentrations at the median value $\bar{c}(M, z)$ and 2σ above the median, respectively; red and blue contours represent $10^{10}\,\mathrm{M}_\odot$ subhaloes, again at the median and 2σ above the median, respectively. The 'x' markers denote the 'true' values for these parameters for the median concentration cases, while the '+' markers denote the true values for the high-concentration cases.

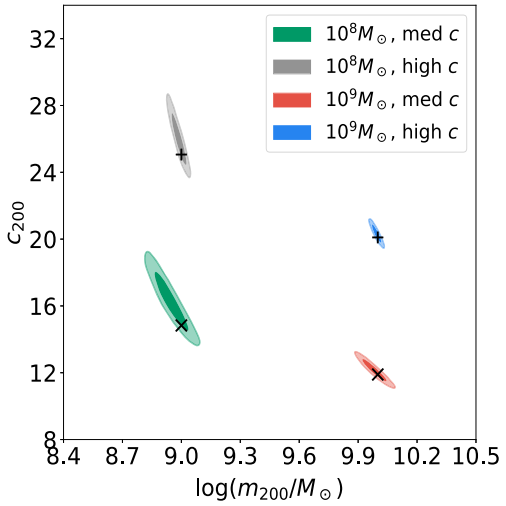

Figure 3. Joint posteriors in log-mass $\log(m_{200}/\mathrm{M}_\odot)$ and concentration c_{200} of 10^8 and $10^9\,\mathrm{M}_\odot$ perturbing subhaloes, inferred using high-resolution simulated images with pixel size ∼0.01 arcsec and PSF width equal to twice the pixel size. Green and grey contours represent posteriors for $10^8\,\mathrm{M}_\odot$ subhaloes with concentrations at 2σ below the median value $\bar{c}(M, z)$ and equal to the median value, respectively; red and blue contours represent $10^9\,\mathrm{M}_\odot$ subhaloes, again at 2σ below the median and at the median, respectively. The 'x' markers denote the 'true' values for these parameters for the median concentration cases, while the '+' markers denote the true values for the high-concentration cases.

relationship will be explored in detail in Section 5). Although the constraints on concentration are weak for $10^9\,\mathrm{M}_\odot$ subhaloes, there is nevertheless a lower bound on concentration, and this was generally true for all of the fits that satisfy our detection criterion (Section 2). Nevertheless, impressive constraints on the concentration can be obtained for $10^{10}\,\mathrm{M}_\odot$ subhaloes. In the median concentration case for which $c_{\rm true} = 11.9$, we infer a 50th percentile value $c_{\rm fit} = 14.9^{+8.1}_{-5.8}$ where the uncertainties give the 95 per cent credible interval. For the high concentration case where $c_{\rm true} = 20.1$, we infer $c_{\rm fit} = 22.3^{+5.6}_{-4.5}$. Remarkably, these uncertainties are smaller than the expected 2σ scatter in concentration for $10^{10}\,\mathrm{M}_\odot$ haloes. In principle, it follows that even with a small number of such detections at *HST* resolution, one may be able to distinguish between the mass-concentration relation expected in CDM (for subhaloes) versus alternate scenarios such as warm or self-interacting dark matter (if one assumes the standard power-law spectrum of inflationary perturbations).

All of the cases shown in Fig. 2 are for subhaloes whose projected position is just outside the critical curve (by 0.01 arcsec). To investigate the constraints for subhaloes further away from the critical curve, in Fig. 5 we plot the resulting constraints for a high-concentration $10^{10}\,\mathrm{M}_\odot$ subhalo at different positions: the grey contours correspond to a subhalo at the innermost position, 0.13 arcsec inside the critical curve; red contours are for a subhalo close to the critical curve (same as blue contours in Fig. 2); blue contours are for a subhalo at the outermost position, 0.15 arcsec outside the critical curve. Interestingly, the constraints for the outermost subhalo (blue) are nearly as good compared to the subhalo close to the critical curve, whereas the uncertainties are significantly weaker for the innermost subhalo. Nevertheless, significant constraints are obtained in each of these cases.

Finally, we note in passing that constraining the concentration may also help in determining whether the perturber is indeed a subhalo or an unassociated halo along the line of sight to the lens. Despali et al. (2018) have shown that it is possible in principle to constrain the redshift of a perturber for strong perturbations, due to the non-linear effects of multiplane lensing. For weaker perturbations where the inferred redshift is somewhat degenerate with the perturber's mass, varying the concentration as an additional model parameter may aid in this determination, since subhaloes may be significantly more concentrated than field haloes of similar mass (Moliné et al. 2017). The interplay between inferences of mass, redshift, and concentration of perturbing haloes is left to be explored in future work.

3.2 Mass–concentration constraints at high resolution

Although the constraints on concentration are weak for $\lesssim 10^9\,\mathrm{M}_\odot$ subhaloes at *HST* resolution, we can ask whether better constraints will be possible for higher resolutions, e.g. using long-baseline interferometry or next-generation very large telescopes. To investigate this, we simulate lenses similar to those shown in Fig. 2, but with 10^8 and $10^9\,\mathrm{M}_\odot$ subhaloes, imaged with pixels four times smaller than *HST* (∼0.013 arcsec compared to ∼0.049 arcsec for *HST*) and assuming a Gaussian PSF whose width is twice the pixel size. Note that both the Thirty Meter Telescope and Giant Magellan Telescope will exceed this resolution; in principle the ALMA radio telescope array can reach this resolution at long baseline, although the pixel noise is highly correlated due to the interferometry.

The high-resolution constraints on concentration and mass are shown in Fig. 3. Remarkably, at this resolution the concentration for $10^9\,\mathrm{M}_\odot$ subhaloes can be well constrained even for low concentrations. At median concentration with $c_{\rm true} = 14.83$, we infer $c_{\rm fit} = 15.78^{+2.31}_{-2.08}$, much smaller than the expected scatter in concentration at this mass for ΛCDM. Even more remarkably, meaningful constraints are obtained for $10^8\,\mathrm{M}_\odot$ even at median or low concentrations whereas neither of these subhaloes were even detected to high significance at the *HST* resolution (in fact the low-concentration perturbation was not detected at all). The latter results should be interpreted with caution, since it is possible that if the

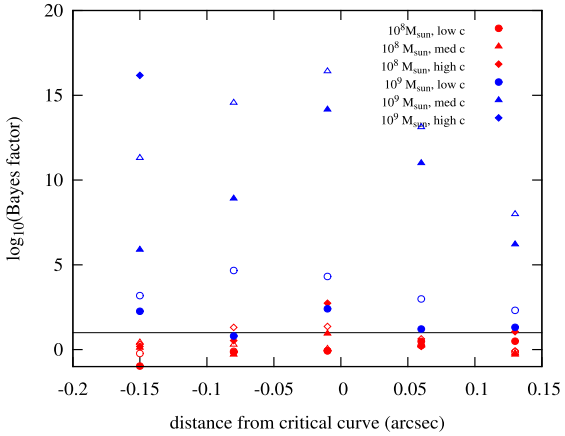

Figure 4. Log-Bayes factors $\log_{10}K$ versus distance from the critical curve for the subset of mock data at $z_{\rm lens} = 0.2$, shown up to $\log_{10} K = 20$ (all $10^{10}\,{\rm M}_\odot$ subhaloes exceed this range and therefore are not shown). The black line represents the threshold for which we consider a subhalo 'detection' to have occurred, corresponding to $\log_{10} K \gtrsim 1$. Filled markers denote the lenses for which the 'small' source galaxy is being lensed, while open markers correspond to the 'large' source being lensed (with unlensed widths given by 0.03 and 0.06 arcsec, respectively). The distances are measured from the nearest point on the *unperturbed* critical curve, with negative values lying outside the critical curve and vice versa.

source model is allowed more freedom than in our model (e.g. for pixelated sources), perturbations as small as $10^8\,{\rm M}_\odot$ might be at least partially absorbed into the reconstructed source, possibly weakening the constraints; on the other hand, source galaxies with detailed internal structure (such as bright pockets of star formation observed in dusty star-forming galaxies; Hezaveh et al. 2016a; Shu et al. 2016) may allow for stronger constraints if this can be captured in the source model. Since pixelated source inversions are computationally intensive, we do not investigate these possibilities here. Nevertheless, we conclude that significant constraints on the mass–concentration of perturbing subhaloes, possibly down to $10^8\,{\rm M}_\odot$, will be possible for next-generation telescopes that attain resolutions $\sim$0.01 arcsec or better.

4 DETECTIONS

To examine which subhalo perturbations are actually detectable, in Fig. 4 we plot the logarithm of the Bayes factor, $\log_{10}K$, against the subhalo distance from the (unperturbed) critical curve for a subset of lenses from our mock data runs. The dashed line represents our detection criterion, namely $\log K > 1$; all cases where $\log K$ is greater than 20 are not shown in the plot (this includes all subhaloes with mass $10^{10}\,{\rm M}_\odot$). Red markers denote $10^8\,{\rm M}_\odot$ subhaloes, while blue markers denote $10^9\,{\rm M}_\odot$ subhaloes. We only show the subset of concentrations with $\Delta_c = (-2, 0, 2)$, (i.e. 2σ below the median, at the median, or 2σ above the median); these are denoted by circles, triangles, and diamonds, respectively. Filled markers denote lenses generated using the 'small' source galaxy, while open markers correspond to the 'large' source galaxy.

Note that nearly all $10^9\,{\rm M}_\odot$ subhaloes are unambiguously detected, with the exception of the low-concentration subhaloes with small sources – these hover near the threshold of detectability, unless very close to the critical curve. This does not mean that the subhalo does not perturb these small sources noticeably (it certainly does), but rather the perturbation is small enough that it can be degenerate with the parameters governing the primary lens. In addition, because the primary lens parameters are less well constrained with the small source, there is more freedom to vary them and possibly mimic the subhalo perturbation. However, we can conclude that all $10^9\,{\rm M}_\odot$ perturbations with large sources and/or concentrations at or above the median are apparently detectable at *HST* resolutions, at least if they lie within $\sim$0.1 arcsec from the critical curve. One important caveat should be given here, however: for the fits in this section, the source was modelled as a Gaussian without Fourier modes. If more freedom is allowed to the source (e.g. with Fourier modes, or with a pixelated source), it is possible that a few of these cases may be well modelled without a subhalo, since the perturbation may be absorbed into the source itself while still achieving a good fit.

For $10^8\,{\rm M}_\odot$, the story is very different: at most a few subhaloes were unambiguously detected, with the clearest detection occurring when the subhalo has a high concentration, is perturbing a small source, and is very close to the critical curve. In general, the smaller source galaxy is more favourable for detection due to the small size of the perturbation: a rapid variation in surface brightness is required for the perturbation to be noticeable at all, unless the concentration is quite high (as the open diamonds show). We conclude that relatively few (if any) $10^8\,{\rm M}_\odot$ subhaloes will be detected at *HST* resolutions in CDM, and those that are detected are very likely to have high concentrations; again however, it is possible that with a more flexible source model, even these cases may be well modelled without a subhalo.

At the higher lens redshift, $z_{\rm lens} = 0.5$, the results are essentially the same, hence we omit the figure for this case. We note however that most of the Bayesian evidences are slightly lower compared to $z_{\rm lens} = 0.2$. Indeed, nearly all of the subhalo perturbations are less pronounced at higher redshift, due to the fact that the angular size of the NFW scale radius is smaller at higher redshift. Since the ratio of angular diameter distances $D_{\rm lens}(z = 0.5)/D_{\rm lens}(z = 0.2) \approx 0.5$, the scale radius at the higher redshift appears smaller by nearly this factor (although not precisely, since haloes have lower concentrations at higher redshift). Thus the noticeable extent of a subhalo's perturbation is smaller at high redshift, at least for a primary lens of fixed Einstein radius. As a result, *none* of the $10^8\,{\rm M}_\odot$ subhaloes were unambiguously detected at $z_{\rm lens} = 0.5$, even if placed very close to the critical curve. Nevertheless, nearly all $10^9\,{\rm M}_\odot$ subhaloes are detected, with the exception of the low-concentration + small source cases with subhalo placed at the extreme positions inside or outside the critical curve.

These results imply that with *HST*-like resolution, perturbing subhaloes of mass $< 10^9\,{\rm M}_\odot$ are more likely to be detected if they have a concentration at or above the median expected value for ΛCDM. For $\sim 10^8\,{\rm M}_\odot$ subhaloes, *only* high-concentration subhaloes have a chance to be detected, and only if they are quite close to the critical curve; for $z_{\rm lens} \gtrsim 0.5$, detection of such low-mass subhaloes is unlikely in any configuration.

5 PHYSICAL INTERPRETATION OF THE DEGENERACY BETWEEN CONCENTRATION AND MASS

Note that the correlation in the inferred concentration versus mass is slightly different in the posteriors for each subhalo position in Fig. 5, with noticeably different 'tilt'. What determines this correlation? In Minor et al. (2017) we showed that for subhalo perturbations, a characteristic perturbation radius can be defined within which the subhalo's projected mass is determined robustly, provided the log-slope of the primary galaxy's density profile is also well determined. This subhalo perturbation radius $r_{\delta c}$ is defined as the projected

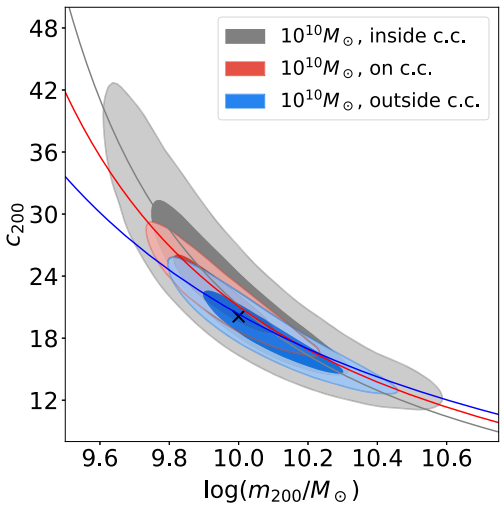

Figure 5. Joint posteriors for a $10^{10}\,\mathrm{M}_\odot$ perturbing subhalo, at different projected positions with respect to the critical curve (and $z_{\rm lens} = 0.2$). Grey, red, and blue contours correspond to subhaloes located 0.13 arcsec inside, 0.01 arcsec outside, and 0.15 arcsec outside the critical curve, respectively. The 'x' marks the true values for these parameters. The solid curves represent the set of points [$\log(m_{200})$, c_{200}] for which the subhalo contains the same projected mass within the perturbation radius $r_{\delta c}$ of the best-fitting model in each case.

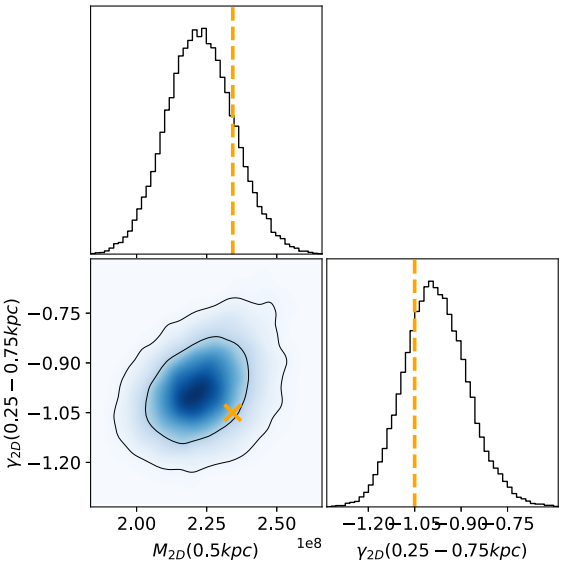

Figure 6. Joint posterior in the projected subhalo mass within 0.5 kpc, $M_{\rm 2D}(0.5\,\mathrm{kpc})$, versus the average log-slope of the density profile from 0.25 to 0.75 kpc, $\gamma_{\rm 2D}(0.25\text{–}0.75\,\mathrm{kpc})$. The mock data were produced with a perturbing subhalo of mass $m_{200} = 10^{10}\,\mathrm{M}_\odot$ and concentration 2σ above the median CDM value, whose posterior in m_{200} and c_{200} is shown as the blue contour in Fig. 2. After fitting the mock data, the subhalo's inferred perturbation radius $r_{\delta c} \approx 0.5$ kpc, so we choose the projected mass and log-slope around this radius as our derived parameters. The actual parameter values are given by the orange marker. Note that, unlike m_{200} and c_{200}, there is no significant degeneracy between these two parameters and the mass is well constrained to within ≈ 10 per cent.

distance from the subhalo's centre to the point where the critical curve is perturbed the most, and to good approximation typically lies along the line from the primary galaxy's centre to the position of the subhalo. To check whether this mass is robustly determined for the $10^{10}\,\mathrm{M}_\odot$ case plotted here, we used the following procedure: first, we calculated $r_{\delta c}$ for the best-fitting model in each case, and the corresponding mass within this radius; next, for an array of m_{200} values over the range of the posteriors, we calculated what concentration is required to keep the mass within $r_{\delta c}$ constant, using a numerical root finder. The resulting curves are plotted in Fig. 5, with colours matching the corresponding posterior. Note that the overall correlation is recovered very well, indicating the perturbation radius is well constrained; the tilts differ because the inferred $r_{\delta c}$ is different in each case, due to the differing subhalo positions.

Since the subhalo's projected mass within the perturbation radius can be determined robustly, another way to cast the results is to infer a derived parameter $M_{\rm 2D}(r_{\delta c,\rm bf})$ where $r_{\delta c,\rm bf}$ is the approximate best-fitting perturbation radius from the fit. Likewise, as a proxy for concentration, one can define a derived parameter $\gamma_{\rm 2D}$ as the average density log-slope in the vicinity of the perturbation radius, since this is the region where the subhalo's perturbation should yield the most information about the profile. For example, in Fig. 6 we plot joint posteriors for the perturbing subhalo of mass $m_{200} = 10^{10}\,\mathrm{M}_\odot$ and concentration 2σ above the median CDM value (whose posterior in m_{200} and c_{200} is shown as the blue contour in Fig. 2). For this subhalo, the best-fitting perturbation radius $r_{\delta c} \approx 0.5$ arcsec, so we choose this radius to evaluate $M_{\rm 2D}(0.5\,\mathrm{kpc})$. We likewise define the average log-slope of the density profile from 0.25 to 0.75, $\gamma_{\rm 2D}(0.25{-}0.75\,\mathrm{kpc})$. Note that there is almost no discernible degeneracy between these two parameters, and $M_{\rm 2D}$ is well constrained to within ≈ 10 per cent. These inferences can be compared to dark matter simulations provided the simulation resolution is sufficiently high to resolve the central density and density slope. Note that, unlike $M_{\rm 2D}$, there is no guarantee that the inferred log-slope will be independent of the subhalo profile chosen; its robustness may depend on the actual interval chosen for evaluating the slope. Nevertheless, the advantage of switching to log-slope is that it is more straightforward to compare to simulations and among different lensing solutions, as it does not depend on defining a theoretical r_{200} or m_{200} for a subhalo. In a companion paper (Minor et al., in preparation), we use exactly this approach when modelling the subhalo detected in the gravitational lens SDSSJ0946+1006 (Vegetti et al. 2010).

Although we have explained how the degeneracy between subhalo mass and concentration arises, we must still understand what determines the inferred limits on the concentration. In Section 8, we will investigate what is physically constraining the subhalo concentration at the high and low ends, and whether tidal truncation significantly alters these constraints.

6 CONSTRAINTS ON SUBHALO PROJECTED MASS, DENSITY LOG-SLOPE, AND POSITION

Now that we have introduced a parametrization of projected mass and density slope for perturbing subhaloes that is largely free of degeneracy (in contrast to m_{200} and c_{200}), we now investigate the constraints on these parameters for the same mock data we explored in Section 4. Here, we focus on subhaloes with mass 10^9 and $10^{10}\,\mathrm{M}_\odot$, since nearly all $10^8\,\mathrm{M}_\odot$ subhaloes were not detected. We will consider subhaloes with concentrations at the median value $\bar{c}(M_{200}, z)$, 2σ below the median, and 2σ above the median (which we will denote by 'med', 'low', and 'high', respectively). We include the mock data with the lenses at $z = 0.2$ as well as $z = 0.5$. As in Section 4, both the mass m_{200} and concentration c_{200} were varied during the fit, and the sources are modelled with Gaussian profiles.

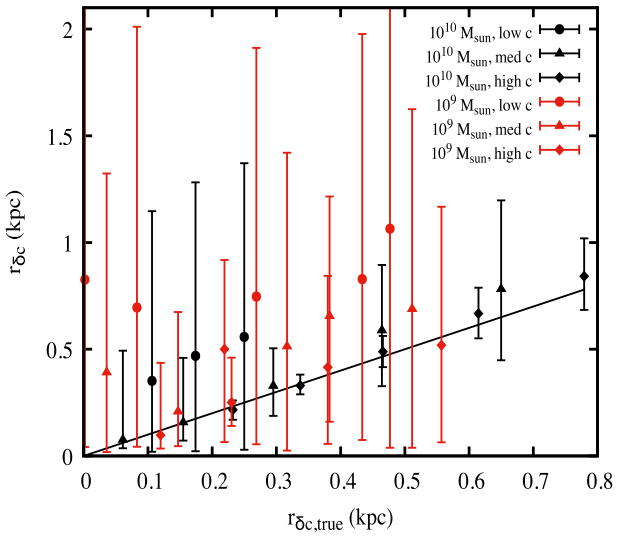

Figure 7. Inferred perturbation radius $r_{\delta c}$, plotted against the true value $r_{\delta c,\mathrm{true}}$ for each of the mock data discussed in Section 6. The point gives the median inferred $r_{\delta c}$, while the error bars give the 95 per cent credible interval. The dashed line denotes the line $r_{\delta c} = r_{\delta c,\mathrm{true}}$. Note that the lowest concentration subhaloes result in the largest uncertainty in the reconstructed perturbation radius.

Before we output derived posteriors in the projected mass and density slope of the subhaloes (using the procedure described in Section 5), we must first get a sense of what the inferred perturbation radius $r_{\delta c}$ is for each perturbation. In Fig. 7, we plot the inferred perturbation radius $r_{\delta c}$ versus the true value, where the points give the median (50th percentile) and the error bars give the 95 per cent credible intervals. From this figure, it is clear that the ability to reconstruct the scale of the perturbation depends as much on concentration as it does on mass: for each subhalo mass, the low concentration perturbers result in the greatest uncertainty in the perturbation radius and vice versa. As we will see shortly, this is partly due to the fact that low-concentration perturbers are harder to locate, i.e. they lead to large uncertainty in the subhalo position; this translates to a large uncertainty in $r_{\delta c}$ since the latter is measured from the centre of the subhalo. Although the $10^9\,\mathrm{M}_\odot$ perturbers generally resulted in larger uncertainties, note that the constraints on $r_{\delta c}$ are better for high-concentration $10^9\,\mathrm{M}_\odot$ than for low-concentration $10^{10}\,\mathrm{M}_\odot$ subhaloes.

Next, to compare the mass/concentration constraints for each group of mock data, we will plot the projected mass and slope near the perturbation radius, as discussed in Section 5. From Fig. 7, we see that 0.5 kpc can be taken as a rough average value for the inferred $r_{\delta c}$; for simplicity, we will therefore plot the inferred $M_{2\mathrm{D}}$ within 0.5 kpc and $\gamma_{2\mathrm{D}}$ over the interval (0.25 kpc, 0.75 kpc), just as we did in Section 5. (Note that since we are not using the exact perturbation radius, this might result in a small amount of bias in $M_{2\mathrm{D}}$ in some cases, but we choose 0.5 kpc for simplicity since here we are primarily interested in comparing the uncertainties, rather than bias.) The results are shown in Figs 8(a) and (b), respectively, where we plot the inferred $m_{2\mathrm{D}}$ and $\gamma_{2\mathrm{D}}$ divided by their true values, against the error in the median recovered subhalo position. Note that, as mentioned above, the low-concentration cases result in the greatest error in the recovered subhalo position. In addition, for each subhalo mass, the higher concentration cases resulted in lower uncertainties in both $m_{2\mathrm{D}}$ and $\gamma_{2\mathrm{D}}$ and vice versa. The $10^9\,\mathrm{M}_\odot$ subhaloes generally yielded poorer uncertainties in $m_{2\mathrm{D}}$ across the board, except most of the high-concentration cases produced better constraints compared to the low-concentration $10^{10}\,\mathrm{M}_\odot$ subhaloes. Strikingly, however, the constraint on the log-slope $\gamma_{2\mathrm{D}}$ correlated more with concentration than subhalo mass: for example, both the median and high concentration $10^9\,\mathrm{M}_\odot$ subhaloes produced smaller uncertainties than the low-concentration $10^{10}\,\mathrm{M}_\odot$ subhaloes.

It should be kept in mind that the uncertainties in Figs 7 and 8 are prior-dependent, not only in the way the subhalo priors are defined, but also in how much freedom is given to the source. It is likely that if a more flexible source model is used, e.g. a pixelated

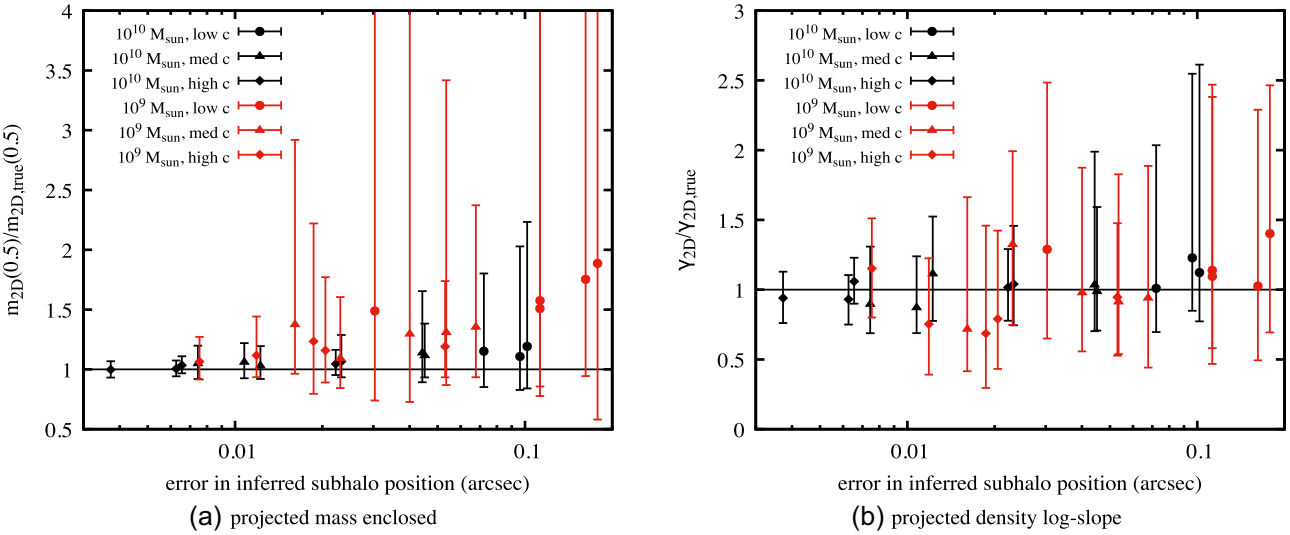

(a) projected mass enclosed

(b) projected density log-slope

Figure 8. Constraints on projected subhalo mass and density log-slope, plotted against the residual in the median inferred subhalo position, for subhaloes of mass $m_{200} = 10^9\,\mathrm{M}_\odot$ and $10^{10}\,\mathrm{M}_\odot$ with varying concentrations and positions with respect to the critical curve. In panel (a), we plot the inferred projected subhalo mass within 0.5 kpc, divided by the true value (point gives the median, while error bars give the 95 per cent credible interval). In panel (b), we likewise plot the average projected subhalo log-slope over the interval from 0.25 to 0.75 kpc. Note that lower concentration subhaloes result in greater uncertainty in the inferred subhalo position, as well as a greater uncertainty in mass and density slope.

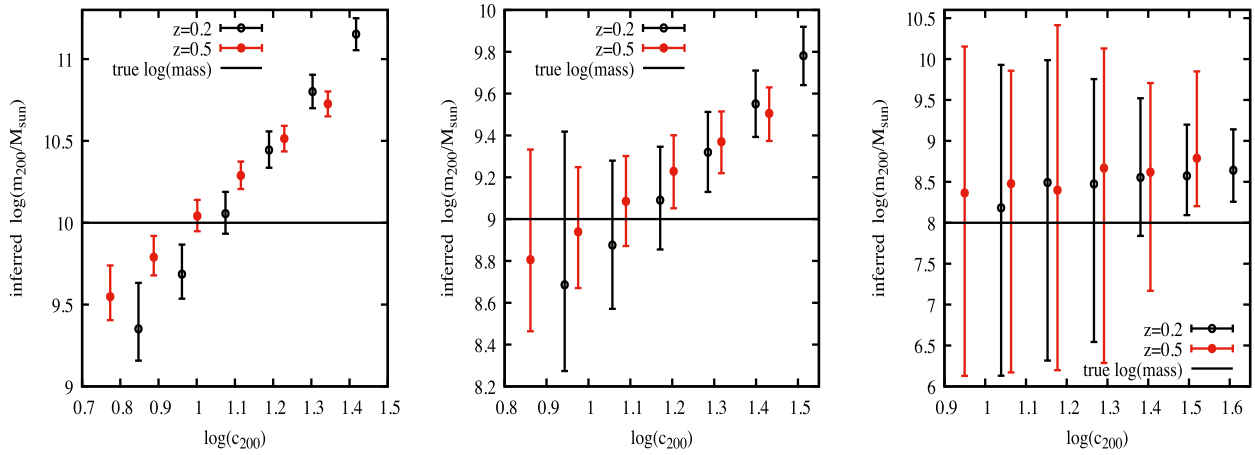

Figure 9. Inferred subhalo mass m_{200} plotted against the subhalo's actual (log) concentration c_{200}, where the modelling assumes the subhalo's concentration to be at the median value for ΛCDM during the fit. Black (red) points show the 50th percentile inferred value for m_{200} for lenses at $z_{\rm lens} = 0.2$ ($z_{\rm lens} = 0.5$), while error bars show the 95 per cent credible intervals. Dashed line shows the subhalo's true mass in each case. The log-concentrations chosen for the mock data (horizontal axis) differ from the median value $\log \bar{c}(M, z)$ by $(-2\sigma, -1\sigma, 0, 1\sigma, 2\sigma, 3\sigma)$ where $\sigma \approx 0.11$ is the scatter in concentration observed in ΛCDM simulations.

source, the uncertainties in m_{2D} and γ_{2D} would become somewhat larger (although in reality, this may not be the case if the source has more complex internal structure compared to our mock sources, allowing for better resolution of the perturbation). Nevertheless, the trends in these figures make clear that the subhalo's concentration plays an important role in how well the subhalo's position, mass, and concentration (or density slope) can be recovered for detectable perturbations.

7 CAN SCATTER IN THE MASS–CONCENTRATION RELATION BE IGNORED WHEN MODELLING SUBHALO PERTURBATIONS?

7.1 Bias in the inferred subhalo mass

Several recent lens modelling studies have modelled subhalo perturbations using an NFW profile, under the assumption that the concentration takes on the median value for ΛCDM, ignoring the expected scatter in subhalo concentrations (Li et al. 2017; Despali et al. 2018; Ritondale et al. 2019). However, Fig. 2 already suggests that the effect can be substantial: for example, if a 10^{10} M$_\odot$ subhalo has a concentration 2σ above the median (the rightmost 'x' in the figure), but one assumes that it has a median concentration (which is a factor of ∼1.7 smaller), the inferred mass indicated by the posterior will be substantially larger. The reason is straightforward: if one underestimates the concentration, then more mass is required to generate a sufficiently large perturbation (this is discussed in detail in Section 5).

Here, we investigate to what extent the inferred mass of a subhalo can be biased due to scatter in concentration, if one assumes the subhalo's concentration is determined by the median value $\bar{c}(M, z)$ expected in ΛCDM. We model all of the mock data described in Section 2.2, varying the subhalo's position and log (m_{200}) parameters while keeping the concentration set to $\bar{c}(m_{200}, z_{\rm lens})$ during the fit.

In Fig. 9, we plot the inferred subhalo mass m_{200} versus the subhalo's actual concentration (or rather, log-concentration) for each of the subhalo masses in our mock data grid (10^{10}, 10^9, 10^8 M$_\odot$ correspond to 9a,b,c, respectively). The circles show the 50th percentile inferred values, while the error bars show the 95 per cent credible interval; black bars are for $z_{\rm lens} = 0.2$, while red bars are for $z_{\rm lens} = 0.5$. In each subplot, recall that the actual concentrations range from being -2σ below the median value, all the way up to 3σ above the median value, with the third bar from the left corresponding to subhaloes at the median concentration. The subhalo was located near the critical curve (at 0.01 arcsec outside) for all the cases plotted. For 10^{10} and 10^9 M$_\odot$, the 'large' source galaxy was used since the uncertainties are somewhat smaller in these cases, whereas for 10^8 M$_\odot$, the small source was used since a greater number of detections occurred in this case.

In Fig. 9(a), one can see that for lenses at $z = 0.2$, 10^{10} M$_\odot$ subhaloes that are 1σ above the median have an inferred mass that is biased high by nearly a factor of 3, while subhaloes 1σ below the median are biased low by a factor of ∼2. At 2σ the bias is even more severe, roughly a factor of ∼6. The corresponding bias at $z = 0.5$ is somewhat smaller, roughly half as large (a factor of ∼3) for concentrations 2σ above the median; this pattern is similar for the 10^9 M$_\odot$ case. For 10^9 M$_\odot$ perturbers (Fig. 9b) the bias is not as severe, but nevertheless m_{200} is biased by a factor of ∼2 for subhaloes whose concentrations are 1σ above the median, and between 3 and 4 for subhaloes 2σ above the median. For 10^8 M$_\odot$, only the subhaloes above the median concentration were detected at all; in these cases however, we see bias of roughly a factor of 3, albeit with large uncertainties.

Although one might expect that very few subhaloes (∼5 per cent) would happen to have concentrations 2σ away from the median, and hence the mass is unlikely to be biased by a factor greater than 2, this may not be the case, for two reasons. (1) Subhaloes tend to have systematically higher concentrations than field haloes, as a result of tidal interactions with the host galaxy; hence, a greater proportion of subhaloes at high concentration is likely. (2) For subhaloes of mass $\lesssim 10^9$ M$_\odot$, high-significance detections are more likely to occur for subhaloes whose concentrations are above the median value. Thus, even in ΛCDM one may expect that the inferred subhalo mass may be biased significantly in many cases, possibly up to a

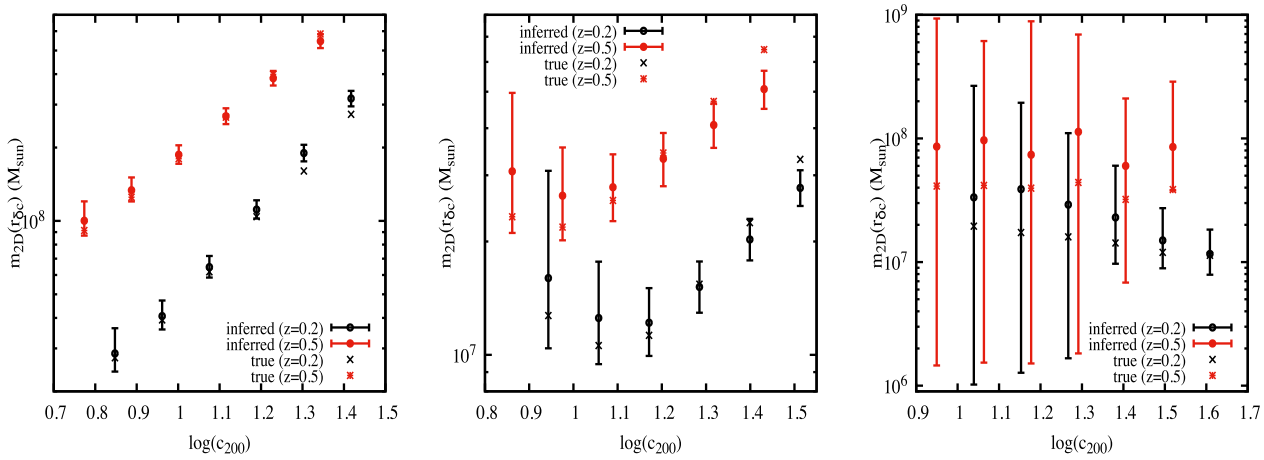

(a) robust mass, $10^{10} M_\odot$ (b) robust mass, $10^{9} M_\odot$ (c) robust mass, $10^{8} M_\odot$

Figure 10. Constraint on the subhalo's projected mass enclosed within its perturbation radius $r_{\delta c}$, plotted against the subhalo's actual (log) concentration c_{200} where the modelling assumes the concentration to be at the median value for ΛCDM during the fit. Plotting conventions are the same as in Fig. 9, except that the corresponding true values $M_{\rm 2D,true}$ are plotted with a black 'x' for $z = 0.2$, and a red asterisk for $z = 0.5$.

factor of 6, if scatter in concentration is neglected when modelling lenses.

Finally, an additional source of bias in the inferred perturber mass comes from the fact that many perturbing haloes may actually be unassociated haloes along the line of sight to the lens, rather than subhaloes (Xu et al. 2012; Li et al. 2017; Çağan Şengül et al. 2020). If the redshift of the perturber differs significantly from the redshift of the primary lens, this may bias the inferred halo mass if unaccounted for during the lens modelling (Despali et al. 2018). In principle, this bias can be quantified using the same methodology in this paper, with a corresponding redshift scaling of the inferred mass [especially the projected mass $M_{\rm 2D}(r_{\delta c})$] depending on the unknown perturber redshift. We leave this analysis to future work.

7.2 Testing the robust subhalo mass estimator

If subhaloes are indeed well approximated by a spherical NFW profile with only modest tidal truncation in most cases, then a straightforward way to overcome the bias in the inferred mass is to vary *both* the mass and concentration as free parameters. In fact, we have seen in Section 3.1 that this approach can yield important constraints about the concentration itself. Nevertheless, it is useful to have a mass estimate that is robust even if the assumed density profile is incorrect (e.g. due to incorrect assumptions about the concentration, tidal radius, or log-slope). In Minor et al. (2017), we showed that a robust mass can be defined in terms of the projected mass contained within the subhalo's perturbation radius $r_{\delta c}$. However, this robust mass estimator was tested using a simulated version of the ALMA lens SDP.81 for which the perturbation radius was very well constrained; this is not always the case for many of our simulated lenses at *HST* resolutions with low-mass or low-concentration perturbations.

Thus, it is useful to test whether this mass estimator – the projected mass enclosed within the perturbation radius – is indeed unbiased for the subhalo fits shown in Fig. 9. To do this, we carry out the following procedure: (1) Calculate the perturbation radius $r_{\delta c}$ as a derived parameter during the nested sampling run. (2) After the run is finished, choose the median (50th percentile) inferred value of $r_{\delta c}$, which we call $r_{\delta c,\rm fit}$ (one could also use the best-fit point for this). (3) For each point in the chain, calculate the subhalo's projected mass enclosed within the radius $r_{\delta c,\rm fit}$, which we call $M_{\rm 2D,fit} \equiv M_{\rm 2D}(r_{\delta c,\rm fit})$; this will be our mass estimator. (4) Plot the resulting posterior in $M_{\rm 2D,fit}$ and compare this to the actual projected mass within the *same* radius, which we call $M_{\rm 2D,true}$. The latter point is important, since the true perturbation radius may differ from our inferred value.

The results of this procedure are shown in Fig. 10. The conventions are similar to Fig. 9, except now we are plotting the mass $M_{\rm 2D,fit}$ and comparing to $M_{\rm 2D,true}$ in each case, marked with an 'x' for $z = 0.2$ (or an asterisk for $z = 0.5$). In nearly all cases $M_{\rm 2D}$ is recovered fairly well: for the 10^{10} $\rm M_\odot$ perturber (Fig. 10a), $M_{\rm 2D,fit}$ differs from the true value by less than 20 per cent in all cases; the same is true for the 10^9 and 10^8 $\rm M_\odot$ perturbers except for the lowest concentration case, for which the bias is 26–27 per cent (albeit still within the error bars). In all cases, the bias in the subhalo's total inferred mass is substantially larger. For example, the 10^9 $\rm M_\odot$ perturber with median concentration infers $M_{\rm 2D}$ with a bias of 8 per cent, whereas the total inferred mass m_{200} is biased by 123 per cent (over a factor of 2). The numbers become starker for higher concentrations: for the cases with concentrations 2σ above the median value, $M_{\rm 2D}$ is biased by a factor of 1.18, 0.90, and 0.99 for $\log m_{200} = 10$, 9, and 8, respectively; the corresponding bias factors in m_{200} are 6.3, 3.6, and 2.6. As expected, the bias in $M_{\rm 2D}$ was greatest in the cases for which the inferred perturbation radius $r_{\delta c}$ differed the most from its true value. However, even in cases where the true $r_{\delta c}$ lay outside the 95 per cent probability region, the inferred $M_{\rm 2D,fit}$ was biased by less than 20 per cent.

We conclude that the mass estimator from Minor et al. (2017) is indeed robust, even at *HST* resolutions where the perturbation radius may be comparable to the pixel size, provided one follows the procedure outlined above. More generally, it has the additional advantage of providing physical insight into what is really being constrained during the lensing, as Section 5 demonstrates. The perturbation radius can be calculated numerically via a standard root-finding algorithm; for details, we refer the reader to section 7.3 of Minor et al. (2017). In this way, $r_{\delta c}$ (and the corresponding subhalo mass enclosed within it) can be incorporated into existing lensing codes if desired and calculated as a derived parameter during lens modelling.

8 DISCUSSION: WHAT REALLY CONSTRAINS THE SUBHALO CONCENTRATION?

In Section 5, we have shown that the correlation between the inferred subhalo mass and subhalo concentration seen in sufficiently large perturbations (Figs 2 and 3) can be explained in terms of the mass enclosed within the perturbation radius being an approximately conserved quantity. However, this cannot be the *only* physical constraint of interest, because it does not explain the upper/lower bounds on the inferred concentration. Here, we discuss the origin of the constraints on the subhalo concentration.

In general, all of the subhaloes that were detected in our mock data, no matter how small, produced a lower bound on the inferred concentration. This is the case even for $10^8\,\mathrm{M}_\odot$ and low-concentration $10^9\,\mathrm{M}_\odot$ subhaloes for which the perturbation radius $r_{\delta c}$ is comparable to the pixel size, and hence is not well constrained. This indicates that the lower bound is not coming from the immediate neighbourhood of the critical curve perturbation, but further out in the lens plane. Indeed, for sufficiently low concentrations, the images are visibly perturbed well beyond $r_{\delta c}$. This can be seen in Fig. 12, where a subhalo with a perturbation radius $r_{\delta c} = 0.14$ arcsec is shown with different concentrations (this is the same $r_{\delta c}$ produced by a $10^{10}\,\mathrm{M}_\odot$ subhalo with concentration 2σ above median, which corresponds to the blue contour in Fig. 2). We plot the resulting images for $c = 2$, 10, 40, 160; note that the subhalo's m_{200} is different in each figure, in order to produce the same $r_{\delta c}$ in each case. If the subhalo has too low of a concentration [$c = 2$, 10 in panels (a) and (b), respectively], the surface brightness far outside the perturbation radius is affected, as well as the overall size of the critical curve itself. To some extent, this can be compensated for by adjusting the primary lens parameters, in particular the Einstein radius and centre coordinates, as well as the source galaxy parameters. However, for low enough concentrations, the subhalo mass must be very large to reproduce the critical curve perturbation scale, and adjusting the primary lens/source parameters is not enough to achieve a good fit.

To demonstrate this, we can simulate and model a perturbation where the subhalo is severely truncated, forcing the perturbation to be more local. We generated a mock image using a truncated NFW profile for a $m_{200} = 10^{10}\,\mathrm{M}_\odot$ (note this is the virial mass in the absence of truncation) with median concentration, and setting the truncation radius r_t to be roughly five times the perturbation radius ($r_\mathrm{t} \approx 0.29$ arcsec, $r_{\delta c} \approx 0.058$ arcsec). We then fit a subhalo with the truncation radius fixed to the correct value, thus forcing the perturbation to be small outside this region. In Fig. 11, we plot the posterior probability in the NFW scale radius r_s, which is a derived parameter, where the black curve denotes the truncated fit. The red curve denotes the probability for an untruncated $10^{10}\,\mathrm{M}_\odot$ subhalo, modelled without truncation, for comparison.[2] The furthest image from the subhalo is approximately 2 arcsec away, and this is roughly the limit on r_s for the non-truncated subhalo. However, the scale radius is allowed to be significantly larger (and thus, lower c_{200}) for the truncated subhalo, since the truncation prevents the perturbation from extending far beyond r_t. In reality, subhaloes are unlikely to be tidally stripped far within r_s without being disrupted altogether. In cases where $r_\mathrm{t} \gtrsim r_\mathrm{s}$, the truncation does not significantly affect the lower bound on c_{200}.

[2]For the untruncated subhalo, we chose the actual subhalo concentration to be slightly lower such that it matches the same perturbation radius ($r_{\delta c}$) as in the truncated subhalo. (Note that because the 3D profile is truncated, the projected density is reduced even near the subhalo centre, reducing $r_{\delta c}$ compared to the same profile without truncation.)

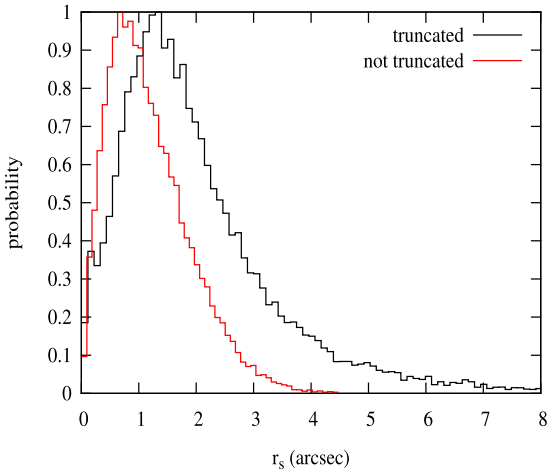

Figure 11. Derived posteriors in the NFW scale radius r_s of a $10^{10}\,\mathrm{M}_\odot$ perturber at $z = 0.2$. Black curve corresponds to a severely truncated subhalo with truncation radius $r_\mathrm{t} \approx 0.29$ arcsec, which was modelled with r_t fixed to this value. Red curve corresponds to a non-truncated $10^{10}\,\mathrm{M}_\odot$ subhalo that generates a perturbation with the same scale $r_{\delta c} \approx 0.058$ arcsec. Note that for the truncated subhalo, r_s is allowed to be quite large (and hence, low c_{200}) because the perturbation is suppressed outside the truncation radius. For most subhaloes r_t will be much greater than $r_{\delta c}$, so significant lower bounds on c_{200} can be obtained.

In contrast to the lower limit on c_{200}, we find that the concentration on the high end is only constrained if the perturbation radius is large enough that the *shape* of the critical curve perturbation can be distinguished. This requires $r_{\delta c}$ to be at least as large as the PSF width (which in our simulations is roughly 0.05 arcsec). Such is the case for all $10^{10}\,\mathrm{M}_\odot$ subhaloes in our mock data, as well as $10^9\,\mathrm{M}_\odot$ subhaloes with concentrations above the median ΛCDM value (for both $z = 0.2$ and $z = 0.5$). This can be seen in panels (c) and (d) of Fig. 12, where the surface brightness in the vicinity of the perturbation (up to a few times $r_{\delta c} = 0.14$ arcsec) can be distinguished between $c = 40$ and $c = 160$, allowing for the concentration to be constrained at the high end for this perturbation scale (blue contour in Fig. 2). Such is also the case for the subhalo perturbing the lens SDSSJ0946+1006, whose concentration is higher than 3σ above the expected median in CDM, generating $r_{\delta c} \sim 0.3$ arcsec as we show in a companion paper (Minor et al., in preparation). However, for our mock data with a $10^9\,\mathrm{M}_\odot$ subhalo with concentration at the median, we have $r_{\delta c} \approx 0.05$ arcsec and there is no significant upper bound on the inferred concentration from the data, as can be seen in Fig. 2 (green contour). When the resolution is increased, as in Fig. 3, the perturbation is better resolved so that c_{200} is constrained even for a low-concentration $10^9\,\mathrm{M}_\odot$ subhalo, while a much stronger upper bound on the concentration is achievable for larger perturbations.

9 EFFECT OF TIDAL STRIPPING ON THE INFERRED MASS–CONCENTRATION OF SUBHALOES

We have seen that the concentration of $10^{10}\,\mathrm{M}_\odot$ subhaloes can be significantly constrained even at *HST* resolution (Fig. 2), while lower mass subhalo concentrations can be constrained at higher resolutions (Fig. 3). However, our modelling up to now has ignored tidal stripping of subhaloes. Since tidal truncation may mimic the effect of having a higher concentration to some extent, here we test whether the mass–concentration constraints are affected by tidal truncation.

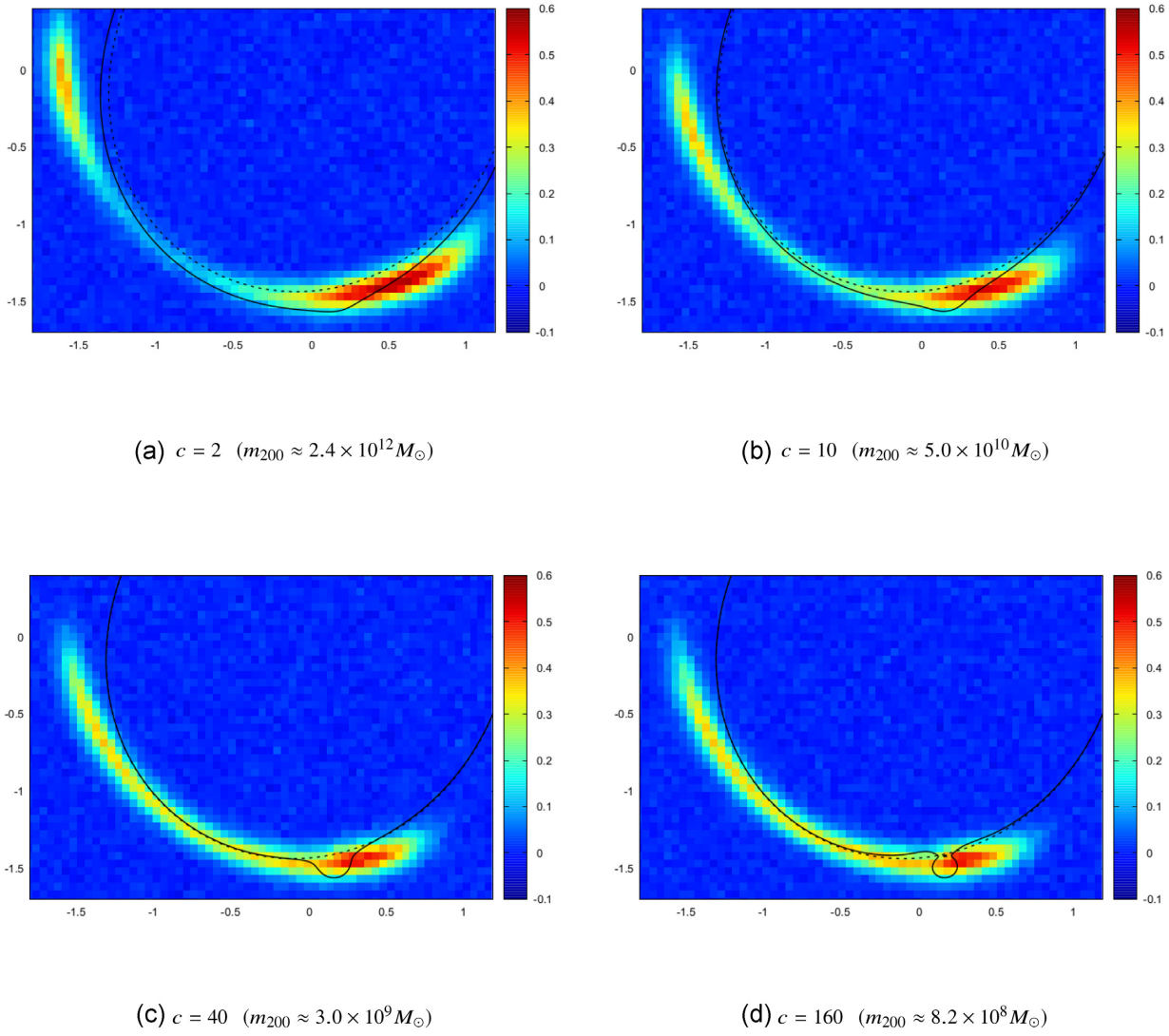

Figure 12. Comparison of the image perturbation produced by a subhalo with perturbation radius $r_{\delta c} = 0.14$ arcsec, for four different concentrations: $c = 2$, 10, 40, 160. For each concentration, the subhalo mass m_{200} is adjusted to produce the same $r_{\delta c}$. Critical curves for the perturbed (solid) and unperturbed (dashed) models are shown for comparison. Note that for low concentrations ($c = 2$, 10), the images are perturbed far beyond the perturbation radius, whereas for high concentrations ($c = 40$, 160) only the immediate vicinity of the perturbation (up to a few times the perturbation radius) is affected. For reference, the perturbation size $r_{\delta c} = 0.14$ arcsec is the same as that produced by a 10^{10} M$_\odot$ subhalo at the same location, with concentration 2σ above the median (blue contour in Fig. 2).

ΛCDM simulations show that tidal stripping results in subhaloes being truncated at or above $r_{\rm max} \approx 2.16 r_{\rm s}$, while few subhaloes are truncated below $r_{\rm max}$ without severe tidal disruption occurring. Hence, we will simulate a truncated NFW subhalo with tidal radius $r_{\rm t} = r_{\rm max}$ and model it with an NFW profile to see whether the resulting m_{200} and c_{200} are biased. For truncated subhaloes, we use the following 'smoothly truncated' profile from Baltz, Marshall & Oguri (2009):

$$\rho(r; r_{\rm s}, r_{\rm t}) = \frac{\rho_0}{\frac{r}{r_{\rm s}}\left(1+\frac{r}{r_{\rm s}}\right)^2\left(1+\left(\frac{r}{r_{\rm t}}\right)^2\right)^2}, \quad (4)$$

where $r_{\rm t}$ is the tidal truncation radius. As our test case, we choose $m_{200} = 10^{10}$ M$_\odot$ and $c_{200} = \bar{c}(M, z)$, solving for the appropriate ρ_0 and $r_{\rm s}$ values for an NFW profile. We then truncate the profile using $r_{\rm t} = r_{\rm max} = 2.16 r_{\rm s}$ and generate simulated data using the same procedure as in Section 2. The effect of truncation on the images is small within the perturbation radius, but quite noticeable outside it; the images near the critical curve are reduced slightly, while the farthest (and least magnified) image is displaced inwards roughly by one pixel length. In addition, the critical curve as a whole is slightly smaller. This begs the question whether subhalo inferences can be significantly biased by fitting a tidally stripped subhalo with an NFW profile without truncation.

To answer this, we fit this mock image assuming an NFW subhalo as in Section 2. Posteriors in m_{200}, c_{200}, and host galaxy Einstein radius b are shown in Fig. 13. Remarkably, there is no apparent bias in m_{200} and c_{200}, despite completely ignoring the tidal truncation; however, the Einstein radius of the primary lens is biased low, in order to reduce the size of the critical curve in the absence of tidal truncation. This is accompanied by a simultaneous slight adjustment of the width and ellipticity of the source galaxy. One can see that in the limit of high concentration and low mass (approximating a truncated subhalo, in a rough sense), the Einstein radius approaches its actual value; in this limit, however, the shape of the critical curve perturbation is noticeably altered in the vicinity of the perturbation

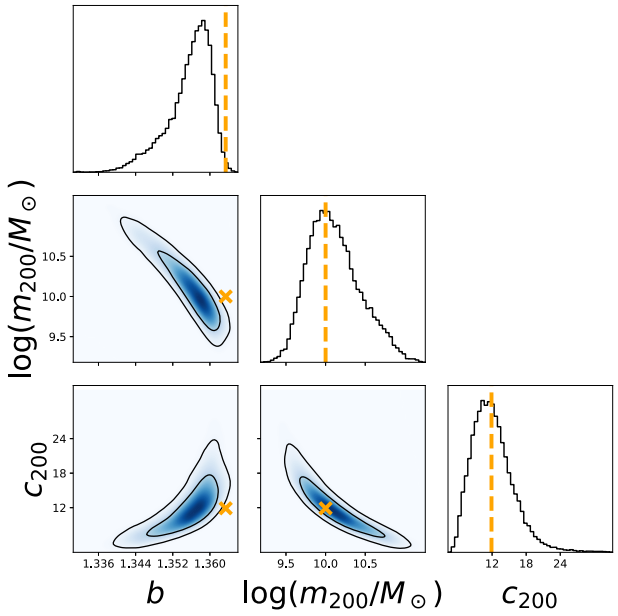

Figure 13. Joint posteriors for a lens at $z = 0.2$ perturbed by a subhalo that is truncated at $r_{\rm max} \approx 2.16 r_{\rm s}$, fit by an NFW profile without truncation. The parameters shown are the host galaxy Einstein radius b, subhalo log-mass $\log(m_{200})$, and subhalo concentration c_{200}. Note that the inferred subhalo mass and concentration are unbiased by the approximation of no truncation, while the host galaxy's Einstein radius comes out biased slightly low to offset the extra mass beyond the subhalo's actual tidal radius.

radius (becoming 'sharper' in appearance), degrading the fit. Hence, the best fit is achieved when the primary lens parameters are slightly adjusted, with the result that there is no discernible bias in the inferred subhalo concentration or mass parameters.

From this, we can conclude that tidal truncation is not expected to significantly bias the inferred subhalo parameters for perturbers with CDM-like concentrations, at least at *HST* resolution. Note that this does not mean that m_{200} is a good approximation to the total subhalo mass: in the example here, the subhalo has $m_{200} = 10^{10}\,{\rm M}_\odot$ but an actual mass $\approx 2 \times 10^9\,{\rm M}_\odot$ due to the tidal truncation. Rather, our results show that the inferred m_{200} and c_{200} parameters themselves are not significantly affected by the truncation. Nevertheless, it is possible that for high-concentration perturbers, the effect of strong tidal truncation (up to $r_{\rm s}$) is more local and not as easily mimicked by adjusting the primary lens model. For very strong perturbations or at higher resolutions, it is therefore advisable to include a tidal radius as a model parameter to reduce bias in the inferred subhalo parameters.

10 CONCLUSIONS

We have demonstrated that the concentrations of dark matter subhaloes perturbing a gravitationally lensed image are an important factor in the strength of the perturbation, allowing for joint constraints on the mass and concentration of subhaloes. At *HST*-like resolutions, we show that the subhalo concentration can be constrained for $\gtrsim 10^{10}\,{\rm M}_\odot$ subhaloes whose concentrations fall within the expected scatter in ΛCDM (Fig. 2); constraints for lower mass subhaloes may be possible if their concentrations are higher than the scatter expected in CDM. Looking to the future, we have shown that constraints on perturber concentration are achievable for $\gtrsim 10^8\,{\rm M}_\odot$ subhaloes at the ∼0.01 arcsec resolution (Fig. 3) attainable by long-baseline interferometry and next-generation extremely large telescopes. This will make it possible to constrain the mass–concentration relation of dark matter haloes on small scales from strong lensing perturbations. This approach is complementary to testing the expected mass function of ΛCDM at dwarf galaxy scales and provides a probe of the small-scale matter power spectrum in addition to dark matter physics.

Likewise, the concentration of perturbers plays an important role in the detectability of the perturbation. We have modelled a large number of mock lenses at *HST* resolution with subhalo perturbations involving a variety of masses and concentrations, in each case fitting a model with versus without a subhalo. For subhaloes with masses of $10^8\,{\rm M}_\odot$, the Bayesian evidence strongly favours a subhalo only if the subhalo is quite close to the critical curve *and* if the concentration is at least 2σ above the expected median value in ΛCDM, indicating only the most concentrated $10^8\,{\rm M}_\odot$ subhaloes are likely to have detectable perturbations. For $10^9\,{\rm M}_\odot$ subhaloes, we find that perturbations are detectable over a broad range of positions (by the same criterion) only if their concentrations are at or above the median value in ΛCDM. In general, we conclude that perturbing subhaloes of mass $< 10^9\,{\rm M}_\odot$ may not be detected unless they have concentrations above the median expected value for ΛCDM.

We have also shown that if scatter in the mass–concentration relation is unaccounted for during lens modelling, the inferred subhalo masses can be biased by a factor of 3 (6) for subhaloes of mass $10^9\,{\rm M}_\odot (10^{10}\,{\rm M}_\odot)$ (Fig. 9). This bias can be eliminated in one of two ways: (1) varying both the concentration and mass as free parameters; and (2) instead of inferring the total mass, inferring the projected mass within the subhalo's perturbation radius, defined by its distance to the critical curve of the lens at the point of maximum perturbation. The latter can be determined much more robustly than the total subhalo mass, with little degeneracy with concentration or density slope, as demonstrated in Fig. 6. In practice, both strategies can be combined, providing constraints on both c_{200} and m_{200} for perturbing haloes under the assumption of an NFW profile, while also providing a robust mass measurement that holds even if the assumed density profile is incorrect (e.g. if a dark matter larger core is present). We use this approach to model the substructure in the lens SDSSJ0946+1006 in a companion paper (Minor et al., in preparation).

Finally, we have shown that for *HST* resolutions, even strong tidal truncation has a negligible bias on the inferred subhalo parameters for high-mass subhaloes with CDM-like concentrations (Fig. 13). We caution, however, that the bias may be more significant for highly concentrated perturbers or at higher resolutions; in such cases, the safest approach may be to include tidal truncation as a model parameter for the subhalo.

As next-generation sky surveys and ground-based extremely large telescopes come online, the ability to measure subhalo concentrations will provide a critical test of the CDM paradigm. The resulting constraints, perhaps in concert with other probes, may provide valuable insights into dark matter physics and the small-scale matter power spectrum.

ACKNOWLEDGEMENTS

We thank the anonymous referee for valuable insights and suggestions that improved this work. We also thank Anna Nierenberg for useful discussions during the course of the project. QM was supported by National Science Foundation grant AST-1615306 and MK by National Science Foundation grant PHY-1915005.

We gratefully acknowledge a grant of computer time from XSEDE allocation TG-AST130007.

DATA AVAILABILITY

No new data were generated or analysed in support of this research.

REFERENCES

ALMA Partnership, 2015, ApJ, 808, L4
Ashoorioon A., Krause A., 2006, preprint (arXiv:hep-th/0607001)
Baltz E. A., Marshall P., Oguri M., 2009, J. Cosmol. Astropart. Phys., 1, 015
Bechtol K. et al., 2015, ApJ, 807, 50
Bose S. et al., 2017, MNRAS, 464, 4520
Brown T. M. et al., 2014, ApJ, 796, 91
Despali G., Vegetti S., White S. D. M., Giocoli C., van den Bosch F. C., 2018, MNRAS, 475, 5424
Dutton A. A., Macciò A. V., 2014, MNRAS, 441, 3359
Elbert O. D., Bullock J. S., Garrison-Kimmel S., Rocha M., Oñorbe J., Peter A. H. G., 2015, MNRAS, 453, 29
Feng J. L., Kaplinghat M., Tu H., Yu H.-B., 2009, J. Cosmol. Astropart. Phys., 2009, 004
Fitts A. et al., 2017, MNRAS, 471, 3547
Garrison-Kimmel S., Horiuchi S., Abazajian K. N., Bullock J. S., Kaplinghat M., 2014, MNRAS, 444, 961
Gilman D., Du X., Benson A., Birrer S., Nierenberg A., Treu T., 2020, MNRAS, 492, L12
Green A. M., Hofmann S., Schwarz D. J., 2004, MNRAS, 353, L23
Hezaveh Y., Dalal N., Holder G., Kisner T., Kuhlen M., Perreault L. L., 2016a, J. Cosmology Astropart. Phys., 048
Hezaveh Y. D. et al., 2016b, ApJ, 823, 37
Kobayashi T., Takahashi F., 2011, J. Cosmol. Astropart. Phys., 1, 26
Li R., Frenk C. S., Cole S., Wang Q., Gao L., 2017, MNRAS, 468, 1426
Lovell M. R., Frenk C. S., Eke V. R., Jenkins A., Gao L., Theuns T., 2014, MNRAS, 439, 300
Minor Q. E., Kaplinghat M., 2015, Phys. Rev. D, 91, 063504
Minor Q. E., Kaplinghat M., Li N., 2017, ApJ, 845, 118
Moliné Á., Sánchez-Conde M. A., Palomares-Ruiz S., Prada F., 2017, MNRAS, 466, 4974
Navarro J. F., Frenk C. S., White S. D. M., 1996, ApJ, 462, 563
Ocvirk P. et al., 2016, MNRAS, 463, 1462
Peng C. Y., Ho L. C., Impey C. D., Rix H.-W., 2010, AJ, 139, 2097
Ritondale E., Vegetti S., Despali G., Auger M. W., Koopmans L. V. E., McKean J. P., 2019, MNRAS, 485, 2179
Rocha M., Peter A. H. G., Bullock J. S., Kaplinghat M., Garrison-Kimmel S., Oñorbe J., Moustakas L. A., 2013, MNRAS, 430, 81
Sawala T. et al., 2016, MNRAS, 456, 85
Shu Y. et al., 2016, ApJ, 833, 264
Suyu S. H., Marshall P. J., Hobson M. P., Blandford R. D., 2006, MNRAS, 371, 983
Vegetti S., Koopmans L. V. E., 2009, MNRAS, 392, 945
Vegetti S., Koopmans L. V. E., Bolton A., Treu T., Gavazzi R., 2010, MNRAS, 408, 1969
Vegetti S., Lagattuta D. J., McKean J. P., Auger M. W., Fassnacht C. D., Koopmans L. V. E., 2012, Nature, 481, 341
Vegetti S., Koopmans L. V. E., Auger M. W., Treu T., Bolton A. S., 2014, MNRAS, 442, 2017
Xu D. D., Mao S., Cooper A. P., Gao L., Frenk C. S., Angulo R. E., Helly J., 2012, MNRAS, 421, 2553
Çağan Şengül A., Tsang A., Diaz Rivero A., Dvorkin C., Zhu H.-M., Seljak U., 2020, Phys. Rev. D, 102, 063502

This paper has been typeset from a TEX/LATEX file prepared by the author.